

Domain Nucleation and Confinement In Agent Controlled Bistable Systems

Dorjsuren Battogtokh*

*Physics and Technology Institute of Mongolian
Academy of Sciences, Ulaanbaatar 51, Mongolia and
Department of Biological Sciences, Virginia Polytechnic
and State University, Blacksburg, Virginia 24061, USA*

(Dated: February 10, 2020)

Abstract

We report a new mechanism of pattern formation in growing bistable systems coupled indirectly. A modified Fujita et. al. model is studied as an example of a reaction-diffusion system of nondiffusive activator and inhibitor molecules immersed in the medium of a fast diffusive agent. Here we show that, as the system grows, a new domain nucleates spontaneously in the area where the local level of the agent becomes critical. Newly nucleated domains are stable and the pattern formation is different from Turing's mechanism in monostable systems. Domains are spatially confined by the agent even if the activator and inhibitor molecules diffuse. With the spatial extension of the system, a larger domain may undergo a wavenumber instability and the concentrations of active molecules within the neighboring elements of a domain can become sharply different. The new mechanism reported in this work can be generic for pattern formation systems involving multistability, growth, and indirect coupling.

PACS numbers: 05.10.-a, 87.17.Aa, 87.18.Hf

* dbattogt@vt.edu;

Turing instability is the most well known mechanism of pattern formation in dissipative systems [1], with the critical condition that the diffusion length of an inhibitor significantly exceeds the diffusion length of an activator [2]. Under this condition, a periodic pattern emerges at a certain critical wavenumber near the stable uniform solution in a monostable system [3, 4]; in a bistable system, periodic patterns can be developed near both of the stable uniform solutions [5], or between the bistable states, depending on initial conditions [6]. Turing patterns can be robust in growing systems [7] and on complex networks [8].

Recently, Fujita et. al. proposed a mathematical model for pattern formation in growing shoot apical meristem (SAM) [9]. The emergence of new stem cell domains, where the concentration of the master protein *WUS* is notably elevated compared to other zones of SAM, is explained by the mechanism of Turing instability. The authors assumed that both active variables, activator and inhibitor, are diffusive in the lateral directions, though there is no clear biological evidence about the diffusive nature of the proteins *WUS* and *CLV1* [9–14]. On the contrary, the experimental observation of sharp discontinuities of *WUS*'s level in adjacent cells [11] suggests that the activator can be non-diffusive or slowly diffusive. A question arises as to whether domain confinement and new domain formation are possible in activator and inhibitor models, in particular in the *WUS-CLV* network, when the classic condition of Turing instability is not fulfilled, because of an intrinsic bistability.

In this work we are concerned with a mechanism of pattern formation in a class of reaction diffusion systems where activator and inhibitor variables can be non-diffusive, but the coupling is carried out by a fast diffusive variable. Such a system was introduced by Kuramoto for indirectly coupled biological cells, and it can be described by the model [15],

$$\begin{aligned}\epsilon \frac{\partial H}{\partial t} &= -H + D_H \Delta_r H + \sum_{j=1}^N w(\mathbf{X}_j) \delta(\mathbf{r} - \mathbf{r}_j), \\ \frac{\partial \mathbf{X}_i}{\partial t} &= \mathbf{F}(\mathbf{X}_i) + g(H(\mathbf{r}_i, t)),\end{aligned}\tag{1}$$

where, $H(x, t)$ is the diffusive variable, \mathbf{X}_i represents the concentrations of chemical molecules in the cell i , N is the number of cells, and \mathbf{F} 's are nonlinear functions. When $\epsilon \ll 1$, $H(r, t)$ is a fast variable whose dynamics are instantly dependent on a component of the vector of concentrations \mathbf{X} , through a function w . Eq. (1) has been studied when the functions $\mathbf{F}(\mathbf{X})$ describe oscillatory dynamics [15, 16].

Let us use the mathematical model of shoot apical meristem by Fujita et. al. in our model of an indirectly coupled system, in the case of a simple linear function for g . By

replacing $\mathbf{F}(\mathbf{X})$ in Eq. (1) with the Fujita et. al. model, our model in spatial dimension one reads,

$$\begin{aligned}\epsilon \frac{\partial H}{\partial t} &= -H + D_H \Delta_x H + \sum_{j=1}^N X_j \delta(x - x_j), \\ \frac{\partial X_i}{\partial t} &= \Phi(E + A_s X_i - B Y_i) - A_d X_i, \\ \frac{\partial Y_i}{\partial t} &= C X_i - D Y_i + S_Y H(x_i),\end{aligned}\tag{2}$$

where the function $\Phi(Z)$ is given by the formula,

$$\Phi(Z) = \frac{A_d u_{max}}{2} \left(1 + \frac{\frac{2Z}{A_d u_{max}} - 1}{\sqrt[n]{1 + \left| \frac{2Z}{A_d u_{max}} - 1 \right|^n}} \right).\tag{3}$$

In Eq. (2-3), E , A_s , A_d , B , C , D , S_Y , u_{max} , and n are positive constants and $\Phi(Z)$ is a sigmoidal function [12] with the values in the range between 0 and $A_d u_{max}$. $H(x_i)$ in Eq. (2) is the H 's value in the cell i . In the absence of H , Eq. (2-3) is the Fujita et. al. model, where X_i represents a hypothetical protein whose expression is controlled by WUS, and Y_i represents the *CLV3* protein in a given cell.

Recent models of SAM suggest the existence of an unidentified diffusive factor in the regulation of SAM [9, 12]. We assume that this unidentified factor is a fast diffusive peptide-hormone, which promotes the synthesis of local inhibitors by quickly sensing the activator concentration in the surrounding medium. We use the wiring diagram of Ref. [13] for the interaction of the factor with WUS-CLV network (Appendix A). In our model, the WUS-CLV network is described by the Fujita et. al. model. For the equation for H , and H 's coupling in the last equation of Eq. (2), we follow Ref. [14] where the diffusive factor is termed as *stemness factor*. X_i in our model represents *WUS*, and Y_i represents the *CLV1/CLV3* complex in a cell layer of SAM. We first assume that both X_i and Y_i are non-diffusive, but the effects of slowly diffusing X and Y will be discussed later.

By assuming a sufficiently dense and uniform distribution of cells [15], the continuity limit of Eq. (2) can be taken. For $\epsilon \ll 1$, H can be expressed by,

$$\hat{H}(x, t) \sim \int_0^L e^{-\frac{|x-x'|}{\sqrt{D_H}}} X(x', t) dx'.\tag{4}$$

Introducing $HS = S_Y \cdot \hat{H}(x, t)$, Eq. (2) is approximated by,

$$\begin{aligned}\frac{\partial X}{\partial t} &= \Phi(E + A_s X - B Y) - A_d X, \\ \frac{\partial Y}{\partial t} &= C X - D Y + HS.\end{aligned}\tag{5}$$

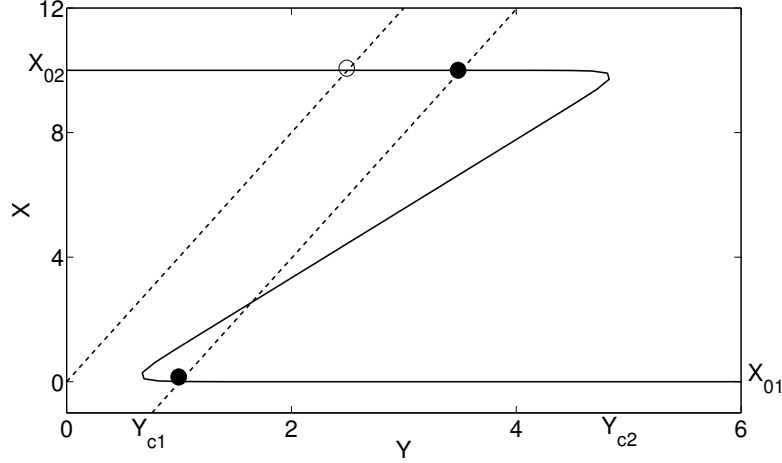


FIG. 1. Nullclines of Eq. (5). Solid line, the nullcline of X . Dashed lines, nullclines of Y . At $HS = 0$, there is a single stable steady solution shown by the open circle. At $HS = 1$, bistable solutions are possible, filled circles. The parameters are: $E = 1$, $B = 2$, $C = 0.25$, $D = 1$, $A_d = 1$, $A_s = 1.9$, $u_{max} = 10$, $n = 20$, and $S_Y = 1$.

In the limit $\sqrt{D_H} \gg L$, where L is the system size, $\hat{H}(x, t)$ can be replaced by the global coupling function of X , $\hat{H}_g \approx \bar{X}$. Then the stationary solutions of Eq. (5) can be found from the intersections of the nullclines with a constant intercept HS , Fig. 1. Y_{c1} and Y_{c2} in Fig. 1 are the saddle-node points for the transition between monostable and bistable solutions, and the corresponding values of the intercepts are, $HS_{c1} \approx D \cdot Y_{c1} - C \cdot X_{01}$ and $HS_{c2} \approx D \cdot Y_{c2} - C \cdot X_{02}$.

We use the term domain for an area in a bistable system, where the local values of a variable are continuously higher or lower than its values in other areas of the system. From a bistable solution, a two-domain solution can be built in extended systems, with the global value $H_g \approx \bar{X}_0 = XL \cdot X_{01} + (1 - XL) \cdot X_{02}$, where XL is the size of the lower domain X_{01} , and $1 - XL$ is the size of the upper domain X_{02} , for $L = 1$. The critical sizes of XL for the existence of a two-domain solution in Eq. (2-3) are $XL_{max} = 1 - \frac{HS_{c1}}{S_Y X_{02}}$ and $XL_{min} = 1 - \frac{HS_{c2}}{S_Y X_{02}}$.

In the interval $H_{c1} \leq HS \leq H_{c2}$, a two domain solution is stable in Eq. (2-3) at the global coupling limit. We seek to illustrate what happens when the coupling range is reduced from global to nonlocal, i.e., $XL_{min} \ll \sqrt{D_H} < L$. In this limit, $HS(x, t)$ can be nonuniform for a two-domain solution in Eq. (2-3), such that it will be higher near the center of the

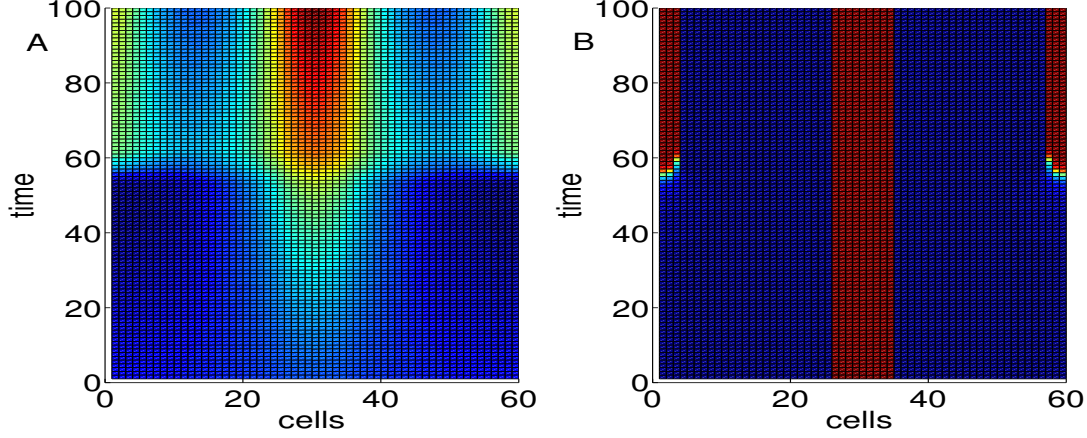


FIG. 2. Domain nucleation in a growing system. Here we assume that the number of cells is fixed but the distances between the cells are increasing at a constant rate. A) Space-time dynamics of H . Higher values of H are shown in red, lower values are shown in dark blue. B) Space-time dynamics of X_i 's. Higher values (near X_{02}) are shown in red, lower values (near X_{01}) are shown in dark blue. Parameters are the same as in Fig. 1, except $D_H = 100$, $\epsilon = 0.01$, $S_Y = 0.5$, $\Delta X_{02} = 1.8$, and $L_0 = 12$.

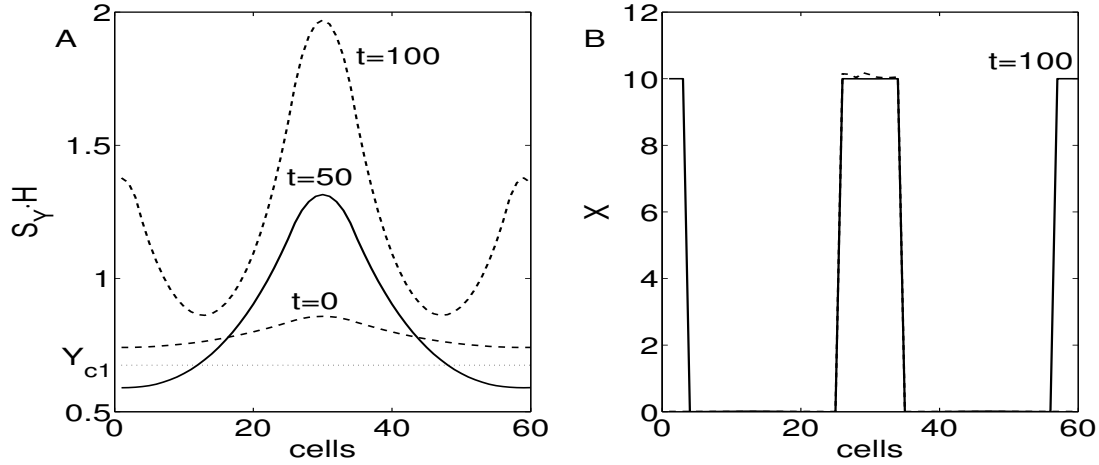


FIG. 3. Snapshots of H and X from Fig. 2 at different time moments. A) Distributions of H . B) Distributions of X_i 's.

upper domain X_{02} , but lower in the areas further away from the center. As the result of the system's growth, it may become possible that in some areas $HS(x, t) < Y_{c1}$ ($HS_{c1} \approx Y_{c1}$, for $D = 1$) but in the bulk of the system $HS(x_{bulk}, t) > Y_{c1}$. In other words, if XL exceeds

XL_{max} as the result of the system's growth, then a domain with the value X_{02} will be nucleated in the area where $HS(x, t) < Y_{c1}$, because X_{02} is the only stable solution below Y_{c1} . After the nucleation, $H(x, t)$ will be quickly adjusted and $HS(x, t) > HS_{c1}$ everywhere. If the intersection of the nullclines is near the point Y_{c2} in Fig. 1, the nucleating domain is X_{01} and consequently $HS(x, t) < HS_{c2}$ everywhere.

To confirm the analysis from Fig. 1, we simulated Eq. (2-3). For detailed numerical simulations of Eq. (2-3), the method proposed in Ref. [17] is more suitable, because when the system size is small and $\epsilon \ll 1$, the finite-difference scheme is stable only at a small time step. We simulated Eq. (2-3) with periodic and no-flux boundary conditions. The initial distributions of X_i 's are chosen such that the X_{02} domain is in the center of the system. For Y_i and H , uniform initial distributions are chosen. The system size is increased in the time interval $t < 50$ as $L = L_0(1 + \frac{t}{25})$, where $L_0 = 12$ is the initial size. After $t \geq 50$ the system size was fixed. Fig. 2 shows a space-time plot of the simulations, and Fig. 3 shows spatial distributions of H and X_i at different time moments. As time increases, the distribution of $H(x, t)$ gets higher in the center of the system, but lower in the areas further away from the center of the system, Fig. 2A. In the areas where the distribution of $S_Y \cdot H(x, t)$ becomes less than the critical value Y_{c1} , new domains are nucleated, Fig. 3A. Similar nucleation patterns as in Fig. 2 can be observed in the simulations with fixed system sizes, for an appropriately chosen system size and initial X_{02} domain.

The distance from the center of the system to the location where a nucleation of the domain takes place is dependent on the size of the initial domain in the center of the system. Assuming the size of the upper domain is ΔX_{02} , an estimate can be made from Eq. (4) for the distance from the initial domain in the center to the location of the new domain,

$$L_{nuc} = \sqrt{D_H} \text{Ln} \left(\frac{2(X_{02} - X_{01} - X_{02} e^{\frac{-\Delta X_{02}}{\sqrt{D_H}}})}{HS_{c1} - 2X_{01}} \right), \quad (6)$$

where $HS_{c1} \sim Y_{c1}$ is defined by the parameters of the model. Numerical simulations are in qualitative agreement with Eq. (6) that the locations of new domains depend on the size of the initial domain ΔX_{02} . In Fig. 4 we plot the results obtained from numerical simulations of Eq. (2-3) at different values of B . The size of the new domain decreases with the increase of ΔX_{02} , whereas, the distance, from the center to the location of the nucleation, increases with the increase of ΔX_{02} . Fig. 4 implies that unlike the Turing patterns in monostable systems, domains in Eq. (2-3) can have different sizes and their distances to each other can

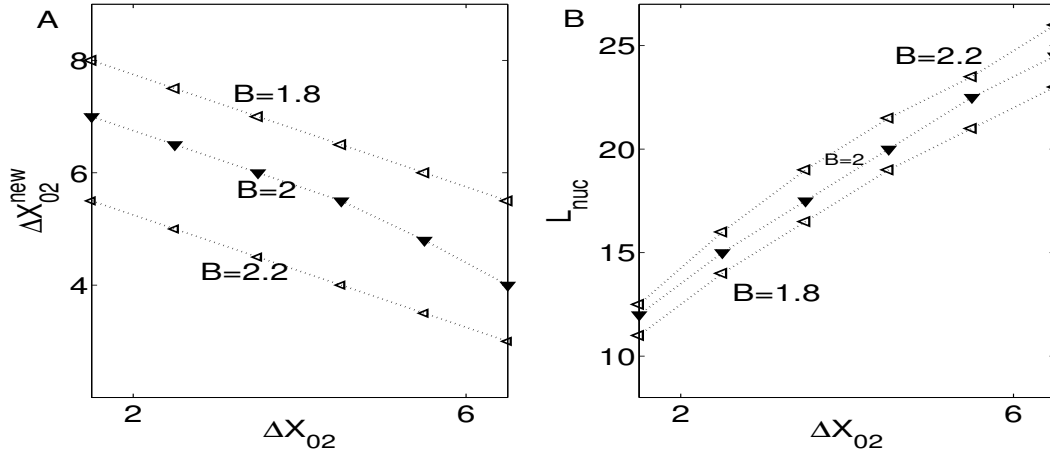


FIG. 4. Domain nucleation at different values of the size of initial domain. A) The size of newly nucleated domain, ΔX_{02}^{new} , vs the size of initial domain ΔX_{02} . B) The distance from the center to the new domain, L_{nuc} , vs the size of initial domain ΔX_{02} . Other parameters are the same as in Fig. 2. The size of the system is fixed at $L = 64$.

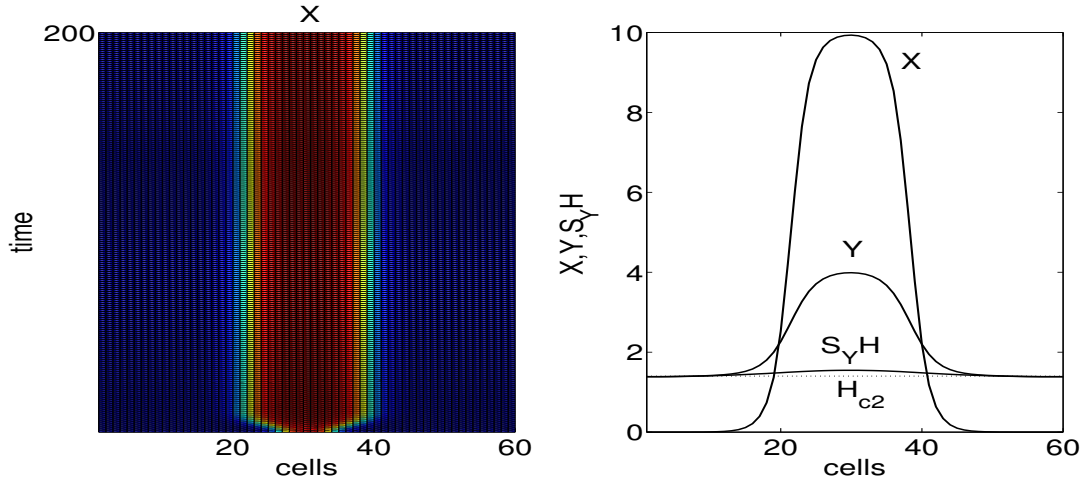


FIG. 5. Domain confinement. A) Space-time plot of X_i 's. B) Snapshots of X_i 's, Y_i 's, and H at time $T = 200$. Parameters are the same as in Fig. 2, except $D_X = 0.1$, $D_Y = 0.1$, and the system size is fixed at $L = 12$.

differ.

A natural question then is whether the domain nucleation in Fig. 2 is possible if X and Y are diffusive. We studied the effects of small diffusion ($D_{X,Y} < 0.3$), by adding the term $DX = D_X(X_{i-1} - 2X_i + X_{i+1})$ into the activator equation of Eq. (2), and $DY =$

$D_Y(Y_{i-1} - 2Y_i + Y_{i+1})$ into the inhibitor equation of Eq. (2). Numerical simulations of Eq. (2-3) with the diffusion terms DX and DY indicate that the domain nucleation is persistent for slowly diffusing activator and inhibitor. This is because a domain in our system can be confined by the agent. Fig. 5 shows the confinement of a domain when X and Y are diffusive. The upper domain in Fig. 5 expands initially, but unlike what is expected from a bistable system with direct coupling [4], the domain does not invade the system. The reason for this is, with the enlargement of the upper domain, due to the diffusion of X_i and Y_i , the field $H(x, t)$ increases everywhere; and as the result, in the area where $S_Y \cdot H(x, t) > HS_{c2}$, the X_{02} state is no longer a stable solution. On the other hand, the X_{01} domain cannot invade the upper domain, because its enlargement lowers $S_Y \cdot H(x, t)$ and stabilizes the X_{02} state. Thus, the domain confinement in our system is the mutual equilibrium of the upper and lower domains, controlled by the agent (Appendix B). This confinement allows nucleation of new domains in growing systems, when X and Y slowly diffuse.

Simulations show that at a stronger coupling strength, a large X_{02} domain loses its stability, and X_{01} states are spontaneously generated. Fig. 6 shows stationary patterns obtained from the simulations with random initial conditions near $X_i \approx X_{02}$ and long-wave distributions of Y_i 's and H . The parameters are chosen such that the homogenous steady state is near the point Y_{c2} in Fig. 1, and it is unstable to nonuniform fluctuations (Appendix C). Instead of stationary Turing patterns near the X_{02} steady state, irregularly distributed X_{01} states are spontaneously generated in the areas where the local values of $H(x, t)$ exceed HS_{c2} . In the absence of X_i and Y_i diffusion, the profile of X_i 's distribution resemble the *chimera state* in nonlocally coupled oscillators [18], Fig 6A. However, if X_i and Y_i diffuse slowly, and $D_X < D_Y$, the pattern is smooth, but large jumps of the activator concentrations between the neighboring cells are possible, Fig. 6B. Interestingly, in the experiments, *WUS* expression in adjacent cells can be sharply different [11].

When $D_H \sim D_{X,Y}$ and the system is in the monostable state near the saddle-node point Y_{c1} , depending on initial conditions, small amplitude Turing patterns can emerge in Eqs. (2-3) via the critical mode selection [6]. With the increase of D_H , the amplitude of these patterns may increase until its maximum and minimum reach the values of the bistable states, such that the pattern behaves like periodic domains in a bistable region (Appendix D). For two variable bistable systems, these regular patterns are possible at $1 \leq \frac{D_Y}{D_X} \leq 6$, unlike for the monostable systems where the ratio is typically larger than 6 for pattern formation

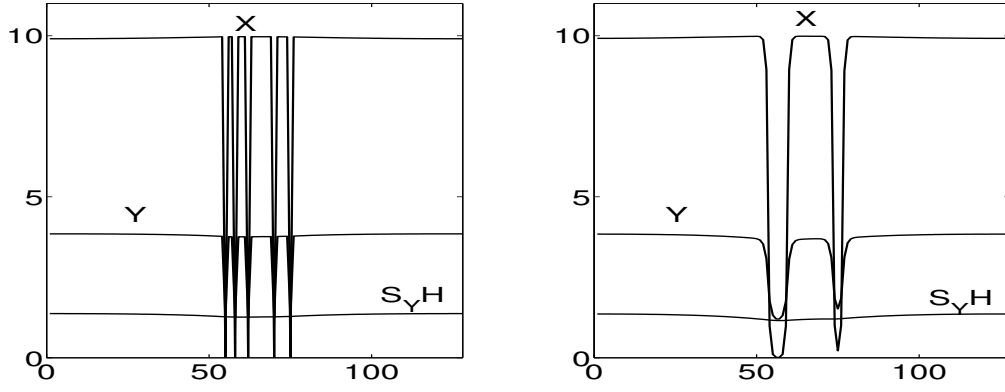


FIG. 6. A domain instability leading to the coexistence of large and small domain solutions. A) Nondiffusive X and Y , B) $DX = 0.035$ and $DY = 0.1$. Parameters are the same as in Fig. 4, except $S_Y = 0.14$, and $B = 2.5$

to be possible. Therefore, the emergence of regular shaped patterns in the bistable region of Eq. (2-3) can be explained by the pattern selection mechanism, as the continuation of the Turing patterns of a homogeneous steady state near the saddle-node points [6]. On the contrary, the size, location, and spatiotemporal dynamics of not only regular patterns, but also of irregular patterns of Eqs. (2-3), in wide range of the parameters and initial conditions, can be explained by the mechanism we described in Fig. 2.

In summary, we studied domain formation and instability in growing bistable systems with a reaction diffusion model, where active variables are non-diffusive but immersed in a medium of a fast diffusive agent. We explained domain nucleation in such a system with a new mechanism. In contrary to the existing theory that explains pattern formation in bistable systems with the Turing mechanism of *nascent* bistability [6], the new mechanism explains it by the intrinsic transitions between coexisting states, controlled by the agent. The new mechanism offers alternative interpretation of existing data and design of next experiments. The experimental data on SAM can be explained in terms of domain nucleation and front bifurcation, not by the critical mode selection of the Turing mechanism. Finally, we believe that the agent controlled pattern formation is generic for developmental biology, involving multistability, growth, and indirect coupling.

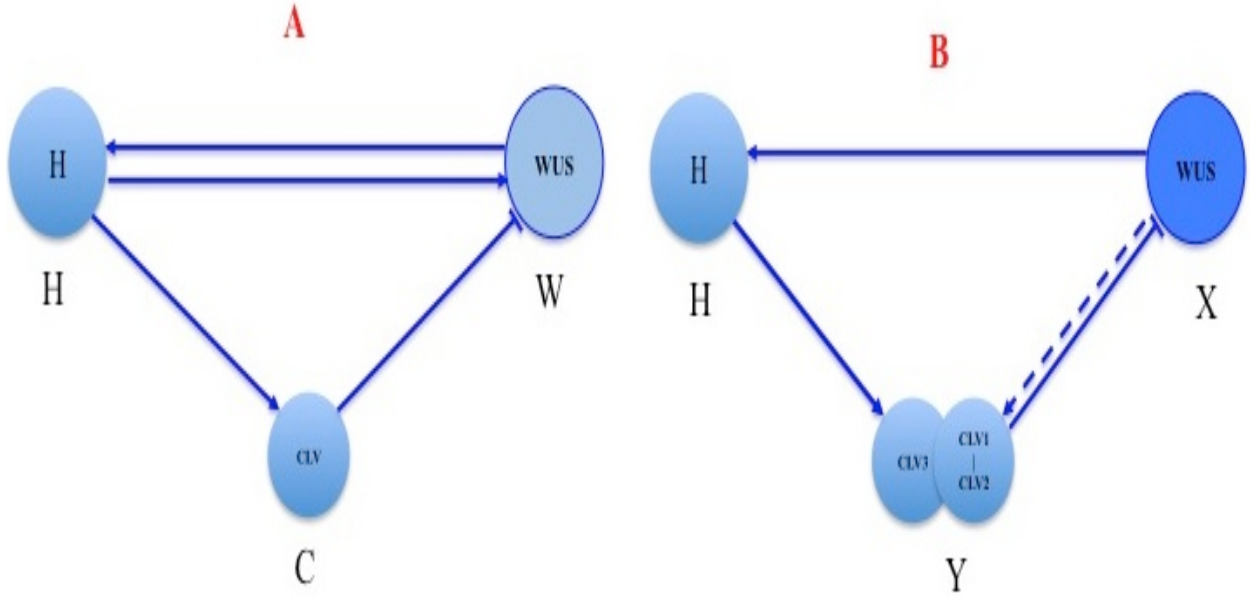


FIG. 7. Wiring diagrams of minimal models of SAM regulation. A) A diagram of a minimal model of SAM regulation by Nikolaev et al [13]. B) A modified version of the diagram. By the intense blue color for *WUS*, we express a self-enhancement mechanism of *WUS*. The dashed line shows an activation of *Y* by *WUS*. The last two features, the characteristics of activator-inhibitor interactions, are adopted from the Fujita et al model [9].

Appendix A: Wiring diagrams and minimal models of SAM

Nikolaev et. al. proposed a minimal mathematical model of SAM. The wiring diagram of the model is shown in Fig. 7. The goal of this simple diagram is to explore the core mechanisms of SAM regulation [13].

The model describes the interactions between *WUS*, *CLV*, and an unidentified factor *H* in the vertical section of SAM, in one dimensional system. It is given by the following ODE's,

$$\begin{aligned}
 \frac{\partial H_i}{\partial t} &= -d_h H_i + (H_{i-1} + H_{i+1} - 2H_i), \\
 \frac{\partial C_i}{\partial t} &= -C_i + g_C(h_C + T_{CH}H_i), \\
 \frac{\partial W_i}{\partial t} &= -W_i + D_W(W_{i-1} + W_{i+1} - 2W_i) + g_W(h_w + T_{WH}H_i + T_{WC}C_i), \quad (A1)
 \end{aligned}$$

where the cell index i goes from $i = 2, 3, \dots, N - 1$, where N is the number of cells. The

boundary cells are described by the following set of equations,

$$\begin{aligned}
\frac{\partial H_1}{\partial t} &= -d_h H_1 + (H_2 - H_1) + g_H(h_H + T_{HW}W_1), \\
\frac{\partial H_N}{\partial t} &= -d_h H_N + (H_{N-1} - H_N), \\
\frac{\partial W_1}{\partial t} &= -W_1 + D_W(W_2 - W_1) + g_W(h_w + T_{WH}H_1 + T_{WC}C_1), \\
\frac{\partial W_N}{\partial t} &= -W_N + D_W(W_{N-1} - W_N) + g_W(h_w + T_{WH}H_N + T_{WC}C_N), \\
\frac{\partial C_i}{\partial t} &= -C_i + g_C(h_C + T_{CH}H_i), i = 1 \& N.
\end{aligned} \tag{A2}$$

In Eqs. (A1-A2), C variable is non-diffusive. The function g describes the interactions between the genes/proteins in Fig. 7, and it is given by a sigmoidal function,

$$g(\xi) = \frac{1}{2} \left(1 + \frac{\xi}{\sqrt{1 + \xi^2}} \right). \tag{A3}$$

For more detailed descriptions and simulations of the model, Eq. (A1-A2), we refer to the Ref. [13]. Here we simulated Eqs. (A1-A2) to show that the model displays dynamics similar to what one would expect from bistable reaction-diffusion systems. Fig. 8 shows stationary distributions of W , C , and H on a cell line of 32 cells. The distribution of W in the stem cell zone of Fig. 8 is reminiscent of a domain in bistable systems, especially when $D_W = 0$, Fig. 8 right plot. Fig. 8 suggests that the argument of the function g , which is a linear combination of the levels of W , C and H fields, can switch the system between bistable states. Therefore, a question arises as to whether the closed forms of the models of SAM with nonlinear functions g (Φ in Eqs. (1-2)) can display an intrinsic bistability. And if so, what are the mechanisms of domain nucleation and domain confinement in the bistable regime? What is the role of bistability in the models of SAM, in particular, in the activator-inhibitor model of Fujita et al?

To answer these questions we modified the wiring diagram in Fig. 7 A to the one shown in Fig. 7 B. We have chosen Fujita et al model because it displays Turing patterns and intrinsic bistability. Following the Fujita et al model, we assume that WUS and Y can be an activator-inhibitor system, where WUS is self-enhancing, and also activating its inhibitor Y . This way we consider the system in the modeling framework of Kuramoto [15], as a reaction-diffusion system, coupled through an indirect, fast diffusive-field, Y .

In Eqs. (1-3) of the main text, the nonlinear function g_X is replaced by Φ ,

$$g_X(\xi) = \Phi(E + T_{XH}H + A_s X + T_{XY}Y), \tag{A4}$$

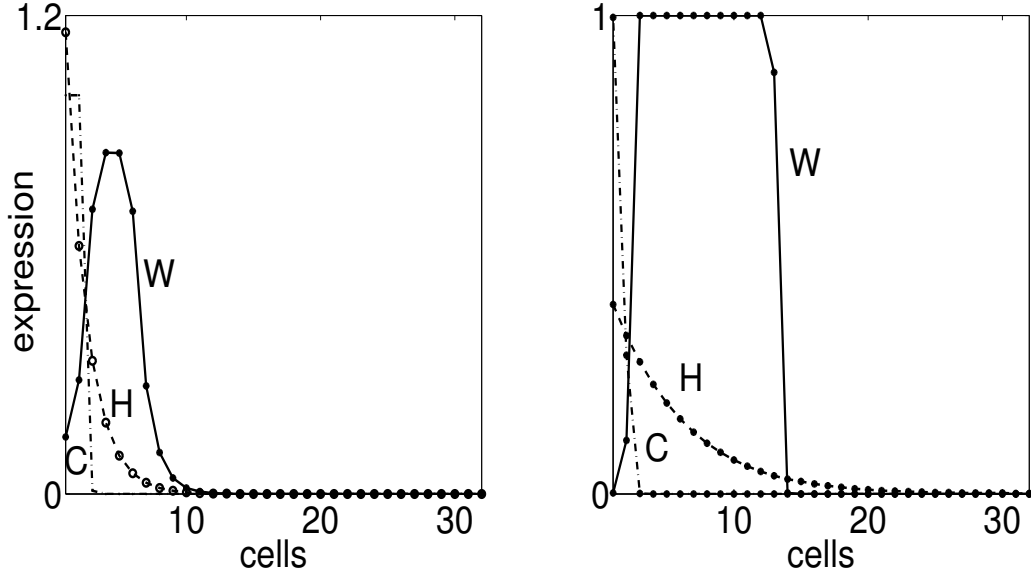


FIG. 8. Simulations of Eqs. (A1-A2). Left: $D_W = 1$. Right: $D_W = 0$. Other parameters are: $h_Y = -0.1$, $h_W = h_C = -88.9379$, $d_h = 0.4$, $T_{WH} = 2500$, $T_{WC} = -2900$, $T_{HW} = 300$, and $T_{CH} = 250$.

where, we assume that $T_{XH} \ll 1$, and $T_{XY} = -B$. Note that $A_d = 1$ in Eq. (2). g_Y is replaced by,

$$g_Y(HS_0 + T_{XY}X + T_{YH}H) \rightarrow HS_0 + CX + S_YH, \quad (\text{A5})$$

where, following Fujita et al [9], we approximate the sigmoidal function g_Y with the linear terms only. Note that $D = 1$ in Eq. (2) of the main text. g_H in our model is replaced by,

$$g_H(h_H + T_{HX}X) \rightarrow X, \quad (\text{A6})$$

where $h_H = 0$. We assume H is a fast variable. As the goal of our model is to study the mechanisms of bistability, domain formation, and domain confinement, we study our model in a closed form.

Appendix B: Domain Confinement

1. Domain Potential

To simplify our analysis, here we study the case of $n = 2$ for Eq. (3) in the main text. Fig. 9 shows a cusp bifurcation in Eq. (5) of the main text, obtained from the continuation

of the saddle-node bifurcation points in Fig. 1 of the main text, using n and B as the principal bifurcation parameters. Fig. 9 shows that at $n = 2$, the bistability is still present, although at $n = 2$, the bistable region is narrow compared to the case of $n > 2$.

For further simplification, we next decouple the first equation in Eq. (5) of the main text from the second equation, by assuming a constant Y , $Y = A_0$. Hence, in the case of a diffusive X , we obtain a single PDE,

$$\begin{aligned} \frac{\partial X}{\partial t} &= f(X, A_0) + \Delta X, \\ f(X, A_0) &= \frac{A_d u_{max}}{2} + \frac{(E + A_s X - B A_0) - 0.5 A_d u_{max}}{\sqrt{1 + \left(\frac{2(E + A_s X - B A_0)}{A_d u_{max}} - 1\right)^2}} - A_d X. \end{aligned} \quad (\text{B1})$$

Eq. (B1) has two stable solutions, X_{01} and X_{02} , which can be obtained numerically by solving the equation $f(X, A_0) = 0$ at different A_0 . From these solutions a table of bistable solutions at different values of A_0 can be built.

The two stable solutions are connected by a front due to the presence of the diffusion term in Eq. (B1). Our goal is to find the condition when the front solution is motionless, i.e. $v = 0$, where v is front velocity, depending on the model parameters. By considering the nonlinear term $f(X, A_0)$ as the forcing term and the diffusion term as the dissipation term, we express $f(X, A_0)$ through its potential by $f = -\frac{dF}{dX}$, where F is given by,

$$F = \frac{A_d X}{2} (u_{max} - X) + \frac{A_d^2 u_{max}^2}{4 A_s} \sqrt{1 + \left(1 - \frac{2(-B A_0 + E + A_s X)}{A_d u_{max}}\right)^2}. \quad (\text{B2})$$

Solid and dashed lines in Fig. 10 show that depending on the parameter $Y = A_0$, the depth of the potential minima can change. The two minima are symmetric at $A_{0c} = 2.05$, which implies that at $A_0 = A_{0c}$, the front is motionless. In the table of pair of stable solutions at different A_0 , the critical value A_{0c} is the one which satisfies the equation $F(X_{01}, A_{0c}) = F(X_{02}, A_{0c})$. The analytic expression for A_{0c} is cumbersome, so we placed the formula for A_{0c} in appendix E.

2. Heteroclinic connection

We confirmed the results shown in Fig. 10 via numerical bifurcation analysis. We transformed Eq. (B1) into two coupled ODE's, by introducing $z = x + vt$ and $X(x, t) = u(z)$,

$$\begin{aligned} u_1'(z) &= u_2(z), \\ u_2'(z) &= v u_2(z) - f(u_1(z), A_0), \end{aligned} \quad (\text{B3})$$

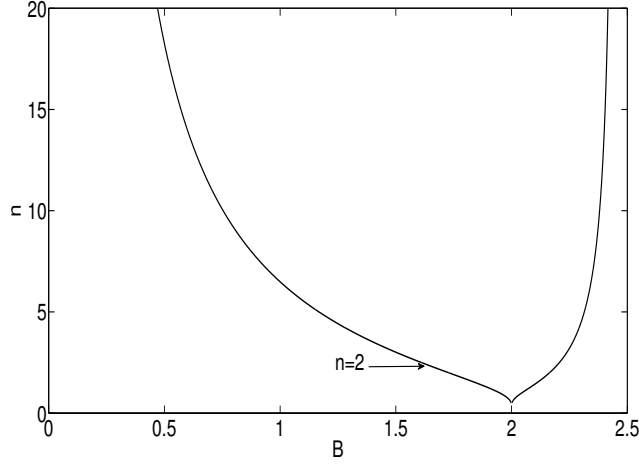


FIG. 9. A cusp bifurcation in Eq. (5) of the main text. Parameters are $A_s = 1.8$, $A_d = 1$, $B = 2$, $C = 0.25$, $D = 1$, $E = 0.1$, $u_{max} = 10$, and $HS = 0.8$.

where $\iota = \frac{d}{dz}$. Eq. (B3) has a pair of stationary solutions (u_{10}, u_{20}) and (u_{11}, u_{21}) . The Jacobian of Eq. (B3) is given by $J = (\{0, 1\}, \{B, v\})$, where $B = (\frac{\partial f(u_1(z), A_0)}{\partial u_1})_{\mathbf{u}_0}$. For the parameters shown in Fig. 10, the pair of solutions (u_{10}, u_{20}) and (u_{11}, u_{21}) are saddle points, as the Jacobian for these solutions have a pair of positive and negative eigenvalues. Using bifurcation analysis software AUTO-07p, we studied heteroclinic connections of (u_{10}, u_{20}) and (u_{11}, u_{21}) , by using A_0 and v as the bifurcation parameters. The bifurcation analysis is in agreement with Fig. 10 that at $A_0 = 2.05$ the front is motionless. Also, the numerically computed velocities via bifurcation analysis and the front velocities computed from the simulations of Eq. (B1) are in perfect agreement, Fig. 11.

3. Global Coupling

Next we consider a case of $A_0 = \kappa \bar{X}$, i. e. the global coupling case, where κ is a constant. The PDE is now given by,

$$\begin{aligned} \frac{\partial X}{\partial t} &= f(X) + \Delta X, \\ f(X) &= \frac{A_d u_{max}}{2} + \frac{2(E + A_s X - B \kappa \bar{X}) - 0.5 A_d u_{max}}{\sqrt{1 + |\frac{2(E + A_s X - B \kappa \bar{X})}{A_d u_{max}} - 1|^2}}. \end{aligned} \quad (\text{B4})$$

When κ and $\bar{X}(x, t_0)$ are small, i.e., $\kappa X(x, t) < A_{0c}$, the potential at the steady state, X_{02} , has a deeper minimum, Fig. 12. Therefore, the front will propagate in the direction

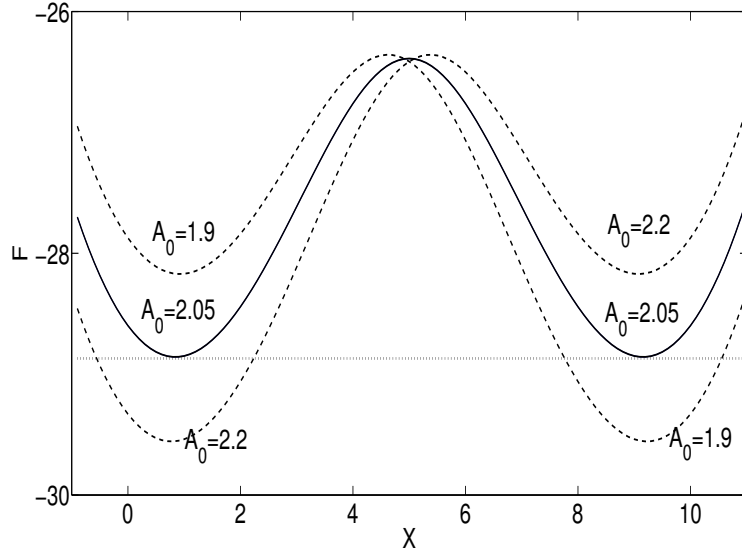


FIG. 10. The potential in Eq. (B2) at three different values of A_0 . When $A_0 < A_{0c} = 2.05$, the front moves in the direction of the expansion of X_{02} solution. When $A_0 > A_{0c} = 2.05$, the front moves in the direction of the expansion of the X_{01} solution. At $A_0 = A_{0c}$, the front is standing. Other parameters are the same as in Fig. 9.

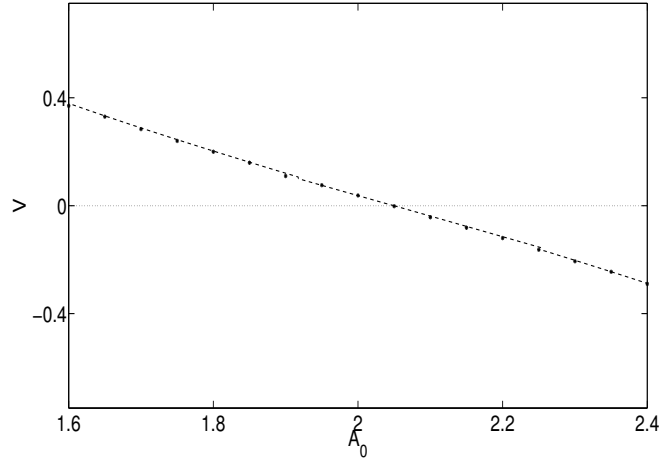


FIG. 11. Front velocity v vs A_0 . The dashed line is obtained via bifurcation analysis of Eq. (B3), as the heteroclinic connections of the steady state solutions. The symbols are obtained from the simulations of Eq. (B1).

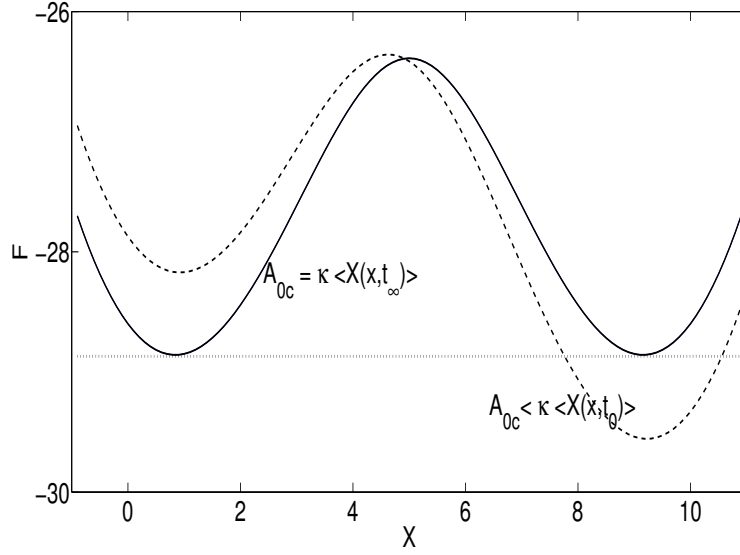


FIG. 12. The potential in Eq. (B2) in the case of global coupling. The parameters are the same as in Fig. 10. When $\kappa\bar{X} < A_{0c}$, the front moves in the direction of the expansion of the X_{02} . Therefore, \bar{X}_{02} increases with time, until the front reaches the point $\kappa\bar{X} = A_{0c}$, where the front is motionless.

of expansion of the X_{02} state Fig. 13, and this process leads to the increase of $\bar{X}(x, t)$. However, the front propagation slows down and eventually stops as it approaches the point where $\kappa\bar{X}(x, t) = A_{0c}$. The final size of the X_{02} domain, i.e. $\bar{X}(x, t_\infty)$, is controlled by the constant κ . If κ is smaller, $\bar{X}(x, t_\infty)$ is larger, and vice versa.

4. A two variable model

Now we consider a two variable model by assuming that $A_0 = S_Y H_0$.

$$\begin{aligned} \frac{\partial X}{\partial t} &= \Phi(E + A_s X - BY) - A_d X + D_X \Delta X, \\ \frac{\partial Y}{\partial t} &= CX - DY + A_0. \end{aligned} \quad (\text{B5})$$

Let us assume that there is a critical value A_{0c} at which the front in the above equation is standing. Then we obtain $Y_0 = \frac{CX + A_0}{D}$. By solving $f(X, A_0) = 0$, with $\Phi(E + \tilde{A}_s X - B\tilde{A}_0)$, where $\tilde{A}_s = A_s - \frac{BC}{D}$, and $\tilde{A}_0 = \frac{A_0}{D}$, we obtain the table of stationary solutions X_{01} and X_{02} at different values of \tilde{A}_0 . The critical value of \tilde{A}_{0c} and the corresponding stationary

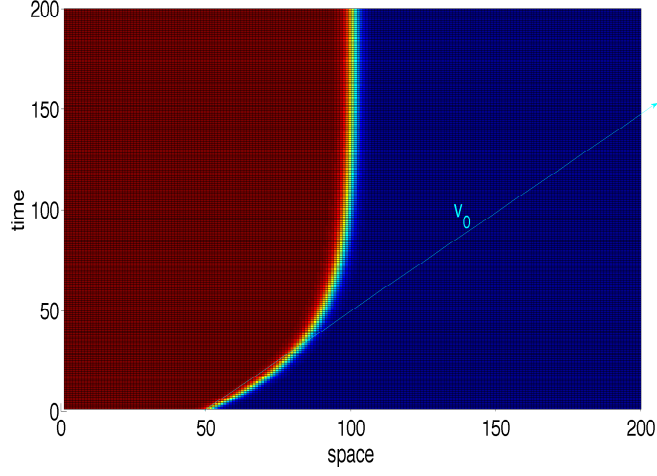


FIG. 13. Domain confinement in the global coupling model, Eq. (B4). In the case for $\overline{\kappa X(x, t)} = \text{const}$, the front propagates with velocity v_0 . However, as $\overline{\kappa X(x, t)}$ increases, the front velocity decreases and eventually becomes zero at $\overline{\kappa X(x, t)} = A_{0c}$. No flux boundary conditions were used for the simulations of Eq. (B4) with the parameters in Fig. 12, except $\kappa = 0.16$.

solutions X_{01} and X_{02} satisfy Eq. (E1). At the critical value of \tilde{A}_{0c} , the front is standing. Note that if Y is diffusive, i. e., if the Y equation of Eq. (B5) has a term $DY = D_Y \Delta Y$, then Eq. (B5) is the continuous limit of the two-variable Fujita et al. model for $A_0 = 0$. At the critical value of $A_0 = A_{0c}$, periodic domain patterns are possible when the ratio $\frac{D_Y}{D_X} \geq 1$. Moreover, if we assume Y to be a fast variable, domain nucleation and domain confinement can be found in such a two-variable model.

5. Domain Confinement in the Three Variable Model

Finally, let us consider the case of diffusive X and Y in the full model,

$$\begin{aligned} \epsilon \frac{\partial H}{\partial t} &= -H + D_H \Delta_x H + X, \\ \frac{\partial X}{\partial t} &= \Phi(E + A_s X - BY) - A_d X + D_X \Delta X, \\ \frac{\partial Y}{\partial t} &= CX - DY + S_Y H + D_Y \Delta Y. \end{aligned} \quad (\text{B6})$$

It can be shown numerically that the same mechanism, based on the equilibrium of the domain potentials, as we have shown above is responsible for the domain confinement, when $\epsilon \ll 1$ and $D_H \gg 1$. Fig. 14 shows the domain confinement in the three variable model,

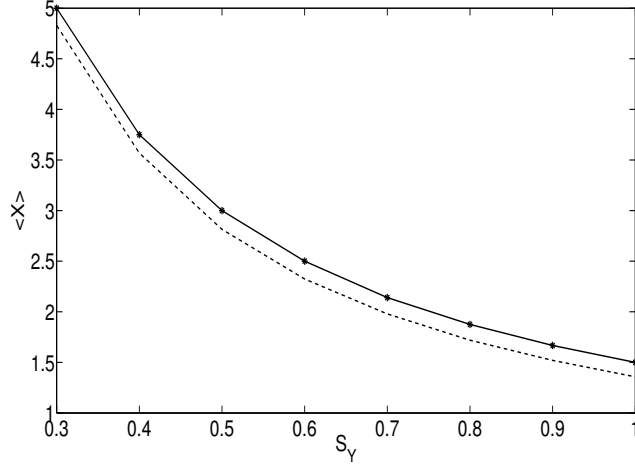


FIG. 14. Domain confinement in Eq. (B5) (solid lines) and Eq. (B6) (dashed lines). Other parameters are the same as in the Fig. 5 of the main text.

Eq. (B6), at different values of the parameter S_Y . The symbols in Fig. 14 were computed using a formula, $\langle X \rangle = \frac{A_0}{S_Y}$, where $A_0 = 1.5$. At this value of A_0 , Eq. (B2) has two symmetric minima. The solid lines were computed from the simulations of Eq. (B5) for $A_0 = S_Y \langle X \rangle$. The dashed lines were computed from Eq. (B6). Other parameters were the same as in the Fig. 5 of the main text. According to Fig. 14, the parameter S_Y controls the size of the confined domain. Thus, these results demonstrate that the fast diffusive field H enforces the domain confinement. It is difficult to explain analytically the domain confinement for $n = 20$, the case of Fig. 5 of the main text and Ref. [9]. However, it can be shown numerically that plots similar to Fig. 14 can be found at large values of n .

Appendix C: Wavenumber Instability

Numerical simulations show that the homogenous steady states (X_{01}, Y_{01}) and (X_{02}, Y_{02}) can be unstable against small fluctuations, and complex patterns can be formed near the saddle-node points SN_1 and SN_2 in Fig. 1 of the main text. The wavenumber instability of the uniform solutions, $\mathbf{X}_0 = (X_{02}, Y_{02})$ (or $\mathbf{X}_0 = (X_{01}, Y_{01})$), can be analyzed by putting the perturbed solutions, $\mathbf{X} = \mathbf{X}_0 + e^{-\lambda t} \cos(qx) \delta \mathbf{X}$, into Eq. (5) of the main text. After standard calculations, the characteristic equation for the stability of the uniform-state is given by,

$$(\lambda - \Phi_x + A_d + D_x q^2)(\lambda + D + D_Y q^2) = \Phi_y (C' + K_y), \quad (C1)$$

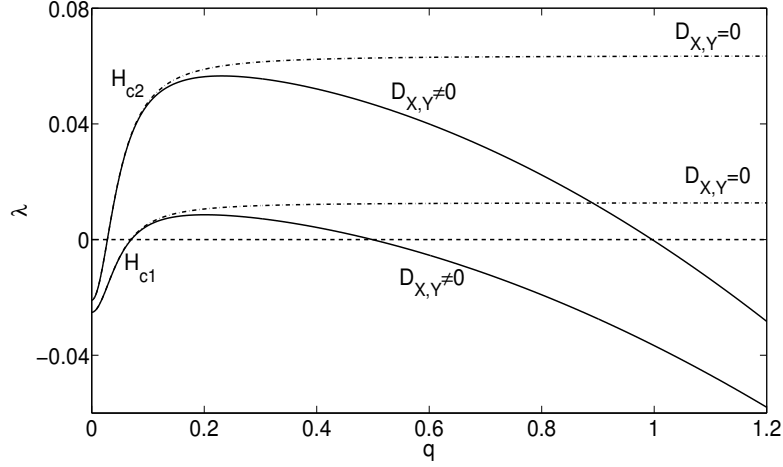


FIG. 15. Linear stability spectra of the uniform states (X_{01}, Y_{01}) and (X_{02}, Y_{02}) near the points SN_1 and SN_2 in Fig. 1 of the main text. Dot dashed lines, $D_X = D_Y = 0$. Solid lines, $D_X = 0.035$ and $D_Y = 0.1$. Other parameters are the same as in Fig. 6 of the main text.

where, $K_y = -S_Y \frac{q^2}{\kappa^2 + q^2}$, $\Phi_z = (\frac{\partial \Phi}{\partial z})_{\mathbf{x}_0}$, $\kappa = \sqrt{D_H^{-1}}$, $C' = C + S_Y$, and $z = (X, Y)$.

In Fig. 15 we show the spectra of λ for the uniform state (X_{01}, Y_{01}) near the point SN_1 , and for the uniform state (X_{02}, Y_{02}) near the point SN_2 . Both spectra are negative at large wavenumbers, if $D_X \neq 0$ and $D_Y \neq 0$. When $D_X = D_Y = 0$, the spectra are positive, $\lambda \geq 0$, at all $q > q_c$, meaning that the neighboring elements can have sharp discontinuities. These two features, $\lambda \leq 0$ at $q \ll 1$ and $\lambda \geq 0$ at $q \gg 1$ imply that sharp discontinuities and extended uniform-like states may coexist in the system. It explains the observation of the *chimera* like states in the simulations. When $D_X \neq 0$ and $D_Y \neq 0$, the spectra are negative, $\lambda \leq 0$, at large wavenumbers $q \gg 1$, meaning that there are no sharp discontinuities of the state variables between the neighboring elements. However, $\lambda > 0$ at certain interval of q in Fig. 15, which implies of the possibility of stationary nonuniform patterns via the Turing mechanism from the monostable states.

In the simulations shown in Fig. 6 of the main text, a wavenumber instability does not lead to stationary Turing patterns near the upper steady state; instead, it may generate states near the lower steady state, if the local values of $H(x, t)$ exceed HS_{c2} . When D_X and D_Y are nonzero, the generated stationary patterns often form irregular domains.

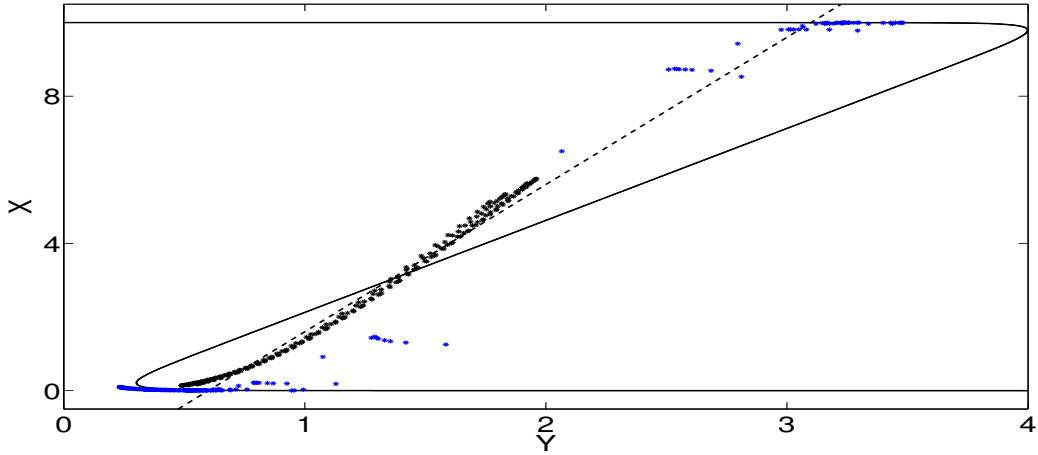


FIG. 16. Periodic patterns are projected on (Y, X) plane. Black symbols: Turing patterns near the saddle-node point HS_1 in Fig. 1. Parameters are: $E = 0.3$, $D_H = 0.36$, and $\delta x = 0.05$. Blue symbols: patterns in the bistable region. Parameters are: $E = 0.1$, $D_H = 100$, and $\delta x = 0.5$. Other parameters are: $B = 2$, $C = 0.25$, $D = 1$, $A_d = 1$, $A_s = 1.8$, $u_{max} = 10$, $D_X = 0.05$, $D_Y = 0.1$, $S_Y = 0.25$, $N = 256$, $\epsilon = 1$, and $n = 20$.

Appendix D: Comparison with Turing Patterns in monostable systems

When $D_H \sim D_{X,Y}$, stationary Turing patterns are possible in Eqs. (2-3). On the (Y, X) plane these regular patterns populate the space in between the bistable states, black symbols in Fig. 16, whereas the patterns that develop for $D_H \gg 1$ connect the bistable states, blue symbols Fig. 16. The black symbols represent regular Turing patterns, with a selected wavenumber, Fig. 17. The blue symbols can be considered as a continuation of the Turing patterns into the bistable region, emerged from a homogeneous monostable state near the saddle-node bifurcation point, Fig. 18. However, in contrast to Turing patterns in monostable systems, there is no clear maximum in the Fourier spectrum for the patterns in the bistable region, where the patterns can become highly irregular due to the interplay with bistability. The size, location and spatiotemporal dynamics of irregular patterns can be explained by the domain confinement mechanism we described above.

Fig. 19 shows two dimensional stationary patterns obtained from simulations with no-flux boundary conditions. The plot on the left resembles Turing patterns, but the plot on the right looks different than typical Turing patterns near the saddle-node points; for example,

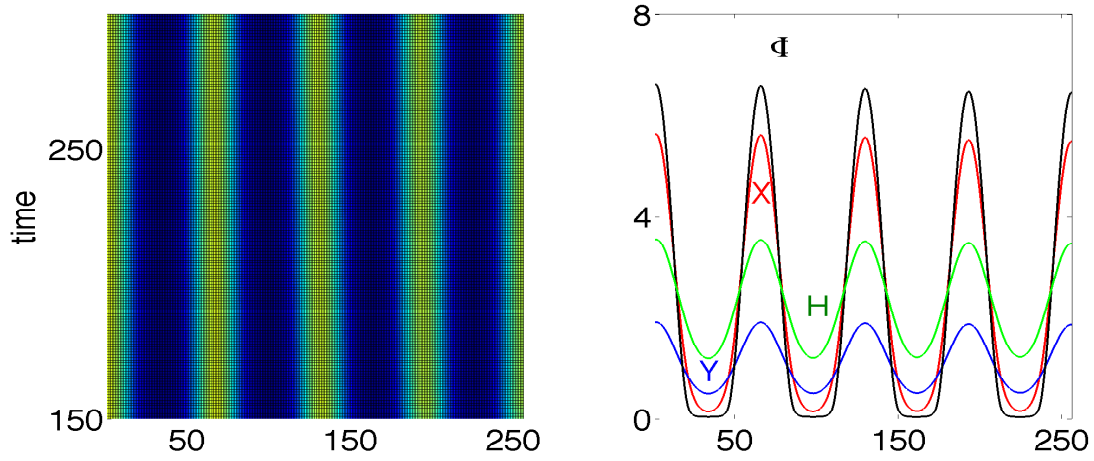


FIG. 17. Space-time profiles of the stationary Turing patterns shown by black symbols in Fig. 16. Formation of the pattern does not involve the mechanism described in Fig. 2.

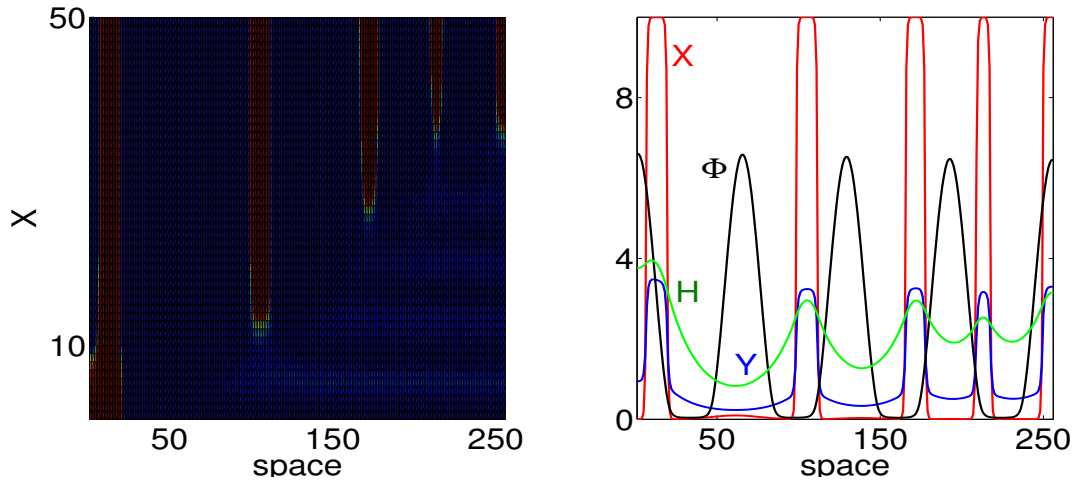


FIG. 18. Space-time profiles of the stationary patterns shown by blue symbols in Fig. 16. Formation of the pattern does involve the mechanism described in Fig. 2.

hexagons or regular spots. These two plots, selected as an example, show that our model can display patterns both similar and dissimilar to the Turing patterns in reaction diffusion systems with monostable states.

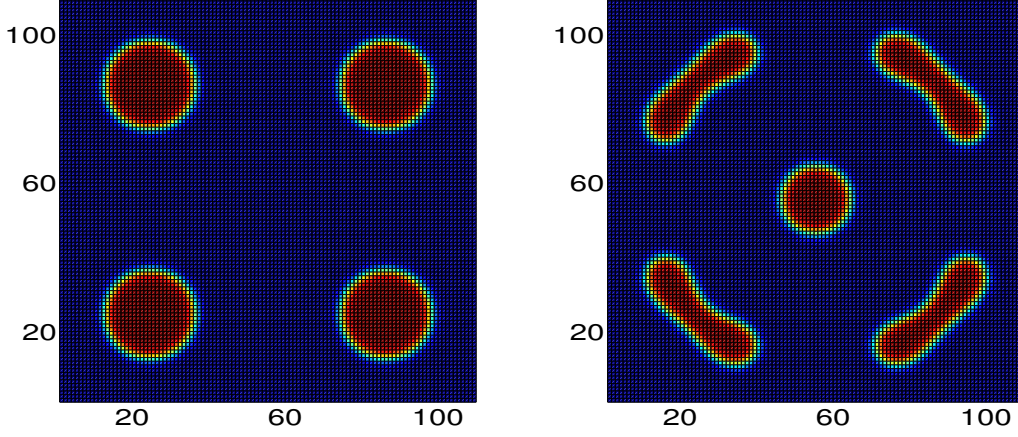


FIG. 19. X patterns in space dimension two for simulations with no-flux boundary conditions. Parameters are: $E = 1$, $B = 2.5$, $C = 0.25$, $D = 1$, $A_d = 1$, $A_s = 1.9$, $u_{max} = 10$, $D_X = 0.3$, $D_Y = 0.3$, $S_Y = 0.5$, $D_H = 100$, and $n = 20$. Left: $\epsilon = 0$, Turing like patterns. Right: $\epsilon = 0.01$, irregular patterns.

Appendix E: Calculation of A_{0c}

The formula for A_{0c} is given by

$$A_{0c} = \frac{1}{2B} \left(2E + \frac{1}{u_{max}^2} (\alpha \pm \beta) \right), \quad (E1)$$

where,

$$\alpha = A_s X_{01}^3 + A_s X_{01}^2 X_{02} - 2A_s X_{01}^2 u_{max} - A_s X_{01} X_{02}^2 + 2A_s X_{01} u_{max}^2 - A_s X_{02}^3 + 2A_s X_{02}^2 u_{max} - A_d u_{max}^3. \quad (E2)$$

In Eq. (E1) β is given by,

$$\beta = (X_{01} + X_{02} - u_{max}) (-A_s X_{01}^2 + A_s u_{max} X_{01} + A_s X_{02}^2 - A_s u_{max} X_{02} + \gamma), \quad (E3)$$

where, γ is given by

$$\gamma = \frac{u_{max}}{(X_{01} + X_{02})(X_{01} + X_{02} - 2u_{max})} \sqrt{\gamma_1 + \gamma_2}, \quad (E4)$$

$$\gamma_1 = -A_d^2 u_{max}^4 + A_s^2 X_{01}^4 - 2A_s X_{01}^3 u_{max} - 2A_s^2 X_{01}^2 X_{02}^2, \quad (E5)$$

$$\gamma_2 = 2A_s^2 X_{01}^2 X_{02} u_{max} + 2A_s^2 X_{01} X_{02}^2 u_{max} + A_s^2 X_{02}^4 - 2A_s^2 X_{02}^3 u_{max}, \quad (E6)$$

ACKNOWLEDGMENTS

I am thankful to Professors A. S. Mikhailov and J. J. Tyson for fruitful discussions.

- [1] A. M. Turing, Philos. Trans. Royal Soc. London, Ser B, **237**, 37(1952).
- [2] A. Gierer and H. Meinhardt, Kybernetik, **12**, 30(1972); H. Meinhardt *Models of Biological Pattern Formation*, Academic Press, London 1982.
- [3] J. D. Murray, *Mathematical Biology II*, Springer-Verlag, Berlin, 2003.
- [4] A. S. Mikhailov, Foundations of Synergetics I. Distributed Active Systems, 2nd revised ed. Springer-Verlag, Berlin, 1994.
- [5] D. Battogtokh, Phys. Rev. E **66**, 066202 (2002); D. Battogtokh, D.A. Browne, Physics Letters A **266** 359(2000).
- [6] S. Metens, G. Dewel, P. Borkmans, and R. Engelhardt, Europhys. Lett., **37**, 109(1997)
- [7] A. Madzvamuse and P. K. Maini, Journ. Comp. Phys. **225**, 100(2007).
- [8] H. Nakao and A. S. Mikhailov, Nature Physics, **6**, 544(2010).
- [9] H. Fujita, K. Toyokura, K. Okada, M. Kawaguchi, PloS One, **6** e18243(2011).
- [10] E. Aichinger, N. Korner, T. Freidrich, T. Laux, Ann. Rev. Plant Biol. **63**, 615(2012).
- [11] S. P. Gordon, V. S. Chickarmane, C. Ohno, E. M. Meyerowitz, PNAS USA, **106**, 16529(2009).
- [12] Jonsson et. al., Bioinformatics **21**, Suppl. i232(2005).
- [13] S. V. Nikolaev et. al., Russ Journ. Dev. Biol. **38**, 383(2007). S. V. Nikolaev et. al., Biofizika, **51**, 583 (2006).
- [14] T. Hohm, E. Zitzler, and R. Simon, PLoS One **12**, e9189(2010).
- [15] Y. Kuramoto, H. Nakao, D. Battogtokh, Physica A, **288**, 244(2000); Y. Kuramoto, Progr. Theor. Phys. **94**, 4352(1996).
- [16] D. Battogtokh, Phys. Lett. A **299**, 558(2002).
- [17] Y. Kuramoto, D. Battogtokh, H. Nakao, Phys. Rev. Lett. **81**, 3543(1998).
- [18] D. M. Abrams, S. H. Strogatz, Int. J. Bifurcation and Chaos **16**, 21(2006); Y. Kuramoto and D. Battogtokh, Nonlinear Phenomena in Complex Systems **5**, 380(2002); D. Battogtokh and Y. Kuramoto, Phys. Rev. E **61**, 3227(2000).